

Supplementary Information for

Full title: Insect-scale jumping robots enabled by a dynamic buckling cascade

Short title: Jumping via Dynamic Buckling Cascade

Yuzhe Wang^{1†}, Qiong Wang^{1†}, Mingchao Liu², Yimeng Qin¹, Liuyang Cheng¹, Ophelia Bolmina¹, Marianne Alleyne³, Aimy Wissa⁴, Ray H. Baughman⁵, Dominic Vella² and Sameh Tawfick^{1*}

1. Department of Mechanical Science and Engineering, University of Illinois at Urbana-Champaign, Urbana, Illinois 61801, United States

2. The Mathematical Institute, University of Oxford, OX2 6GG, United Kingdom

3. Department of Entomology, University of Illinois at Urbana-Champaign, Urbana, Illinois 61801, United States

4. The Department of Mechanical and Aerospace Engineering, Princeton University, Princeton, New Jersey 08544, United States

5. Alan G. MacDiarmid NanoTech Institute, University of Texas at Dallas, Richardson, Texas 75080, United States

[†] These authors contributed equally to this work

*Corresponding author: Sameh Tawfick

Email: tawfick@illinois.edu

This PDF file includes:

Supplementary text
Figures S1 to S6
Tables S1 to S7
Legends for Movies S1 to S6

Other supplementary materials for this manuscript include the following:

Movies S1 to S6

Supplementary Information Text

This Supplementary Information text contains details of tailoring the artificial muscles, the mathematical model used to describe the jumps and determine the effect of the restriction height, as well as details of jumping insects.

Details of tailoring of the coiled artificial muscles

Based on the force-displacement curve of the various snapping configurations, we set two conditions to meet these requirements. The first condition is the combination of the maximum force and stroke at the point of snap-through. This requirement is assessed by measuring the stroke of the muscle in an isobaric test of that required peak force (constant force test). The second requirement is to achieve the maximum force when tested without any pre-load and with displacement-constrained ends. The second requirement is checked by an isometric test setup, similar to what is commonly performed to test musculoskeletal muscles when a health practitioner constrains the displacement produced by the patients' muscles and measures the force that the patient can generate under this constraint. To our knowledge, the combination of these two requirements to match a complex force-displacement response of a mechanism is novel and facilitates the process of muscle tailoring for robot needs.

We constrained our actuators' design space to coiled thermally-powered artificial muscles made of nylon fishing lines. We show three examples of muscles tailored for this robot. The first muscle is a self-coiled muscle made from a 1 mm diameter fiber (please see SI for fabrication details). This muscle barely meets the first requirement, as shown in Fig. 4D, but clearly does not meet the second requirement, which precludes its use for the robots. In fact, it became obvious during this study that one limitation of the self-coiled artificial muscle is that high preloading is needed to separate the coils because of high muscle stiffness. This indicates that a coiled artificial muscle with initially separated coils is needed for this mechanical task. This type of coiled muscle is known in the literature as mandrel-coiled muscle (32), where the fiber (here fishing line) is initially twisted, but instead of self-coiled by twist insertion under a constant load, it is then wrapped around a cylindrical core referred to as the mandrel. This creates a muscle with a larger coil diameter and hence a large spring index (defined as the ratio between the outer coil diameter and the fiber diameter). It is known that larger spring indices muscles have spacing between their coils and provide larger stroke but smaller force (measured in isobaric test). Indeed, a mandrel coiled muscle having a spring index of 3.26 meets both requirements as shown in Fig. 4D. Four of these muscles, called M3 muscles, working in parallel meet the most stringent requirements of robot Sy. These muscles are rather heavy (0.52 g total mass), so we attempted to tailor smaller diameter, lighter weight M2 muscles, and their performance in Fig. 4D and 4E. However, these muscles will uncoil under 4 N of external load and hence are not suitable for the robots. Overall, the energy capacity of these muscles in this use case is the area under the force-displacement curve, which is 8.78×10^{-3} Nm for the Sy robot, corresponding to 4 mJ/g. (We comment further on this energy capacity value in the discussion section.)

Details of the Von-Mises truss model

Equations of motion for different phases

As shown in Fig. 6A of the main text, we consider a central mass connected to two springs, sandwiched between two larger masses; the central mass and springs represent the beam (m_b), while the outer masses represent the robot (m_r). The jump is latched by pushing the central mass to the horizontal position ($y_b = 0$). It then undergoes snap-through, ultimately hitting the substrate when $y_b = -d$, whereupon the robot starts the main portion of the jump. We neglect the weight of the central mass, as it is much lighter than the outer masses (while considering its inertia), but incorporate the weight of the outer (larger) masses, which is necessary to ensure that the robot does not immediately jump.

The essential ingredients of the model are that each mass is subject to a force from the spring, its weight (for the edge masses), and may also be subject to a reaction force from the substrate.

The springs have natural length l_0 and stiffness k (see Fig. 6A (i)), so that the force they exert tangent to themselves is

$$F = k \left\{ \left[w^2 + (y_b - y_r)^2 \right]^{1/2} - l_0 \right\}, \quad (1)$$

where w is the distance between the central (beam) mass and the edge (robot) mass (which is also the half distance between edges of the robot) and $y_{b,r}$ are the vertical displacements of the central and edge masses, respectively. The horizontal component of the forces from the two springs cancel by symmetry; the vertical component gives rise to an equation of motion via Newton's second law applied to the central mass (neglecting its weight), namely:

$$m_b \frac{\partial^2 y_b}{\partial t^2} = -2k(y_b - y_r) \left\{ 1 - \frac{l_0}{\left[w^2 + (y_b - y_r)^2 \right]^{1/2}} \right\} + R_b. \quad (2)$$

Similarly, for each of the edge masses, Newton's second law gives:

$$m_r \frac{\partial^2 y_r}{\partial t^2} = k(y_b - y_r) \left\{ 1 - \frac{l_0}{\left[w^2 + (y_b - y_r)^2 \right]^{1/2}} \right\} - m_r g + R_r, \quad (3)$$

where R_b and R_r are the reaction forces from the substrate on each mass.

These equations are to be solved subject to the initial conditions $y_b(0) = -\epsilon$, $\dot{y}_b(0) = 0$, with the reaction forces determined by the constraint that the masses cannot penetrate the substrate, i.e. $y_r \geq 0$, $y_b \geq -d$. Solving this model, we find that there are four stages of the jump:

1. **Snap-down:** The central mass accelerates towards the floor under the force of the relaxing spring (see Fig. 6A (iii)). In this stage, $R_b = y_r = 0$, so that eq. (2) reduces to

$$m_b \ddot{y}_b = -2ky_b \left[1 - \frac{L_0}{(w^2 + y_b^2)^{1/2}} \right]. \quad (4)$$

We non-dimensionalize by letting $y_b = w \cdot Y_b$, $\lambda = L_0/w$, $\Delta = d/w$ and $t = t^* \cdot T$ with time scale $t^* = \sqrt{m_b/2k}$. Then we have

$$\frac{d^2 Y_b}{dT^2} = -Y_b \left[1 - \frac{\lambda}{(1 + Y_b^2)^{1/2}} \right]. \quad (5)$$

Note that λ is an aspect ratio parameter characterizing the natural length of the spring compared to its length in the latched configuration. For this state to be compressed (rather than stretched), we require $\lambda > 1$. We consider a small perturbation applied to the central mass to initiate the snap-down, i.e.,

$$Y_b(0) = -\varepsilon, \dot{Y}_b(0) = 0. \quad (6)$$

A linear stability analysis suggests that for early times:

$$Y_b(T) \approx -\varepsilon \cosh(\sqrt{\lambda-1} \cdot T). \quad (7)$$

Note that if d is large enough that the system reaches equilibrium $Y_{b,e} < 0$ with: $\lambda = (1 + Y_{b,e}^2)^{1/2}$ (so that $\ddot{Y} = 0$) then the object may not jump at all. Hence, we expect to need $|Y_{b,e}| = \sqrt{\lambda^2 - 1} > \Delta$.

Non-dimensionalizing eq. (3) in the same way as for eq. (2), but further introducing $y_r = w \cdot Y_r$, $\mu = m_r g / 2kw$, $M = m_r / m_b$ and $\bar{R}_r = R_r / 2kw$, we have

$$M \frac{\partial^2 Y_r}{\partial T^2} = \frac{(Y_b - Y_r)}{2} \left\{ 1 - \frac{\lambda}{[1 + (Y_b - Y_r)^2]^{1/2}} \right\} + \bar{R}_r - \mu. \quad (8)$$

Initially, $Y_r = 0$, so we have

$$\bar{R}_r = \mu + \frac{Y_b}{2} \left[\frac{\lambda}{(1 + Y_b^2)^{1/2}} - 1 \right]. \quad (9)$$

Phase 1 continues until $\bar{R}_r = 0$, at which point the reaction force would have to become negative to maintain $Y_r = 0$; since the substrate is not adhesive, instead the edge masses begin to jump, i.e., $Y_r > 0$, $R_r = 0$. This is the beginning of Phase 2 of the motion and occurs when $Y_b = Y_{b,jump}$ with

$$\frac{2\mu}{|Y_{b,jump}|} = \frac{\lambda}{(1 + Y_{b,jump}^2)^{1/2}} - 1. \quad (10)$$

By solving this equation numerically for given parameters μ and λ , we can determine $Y_{b,jump}$, and therefore find that $T = T_{jump}$ at $Y = Y_{b,jump}$.

2. *Ghost jump*: As the central mass accelerates downwards, but before it contacts the substrate, the outer masses are slightly lifted off the ground (see Fig. 6A (iv)). In this second phase of the motion, $R_b = R_r = 0$ with Y_b and Y_r non-zero. (We shall see that in general this motion is a slow acceleration and is short-lived, so it may be neglected in our analytical work; we nevertheless include it for completeness.)

Both central and edge masses are moving (but in different directions). For the central mass,

$$\frac{d^2 Y_b}{dT^2} = -(Y_b - Y_r) \left\{ 1 - \frac{\lambda}{[1 + (Y_b - Y_r)^2]^{1/2}} \right\} \quad (11)$$

and, for the edge masses,

$$M \frac{d^2 Y_r}{dT^2} = \frac{1}{2} (Y_b - Y_r) \left\{ 1 - \frac{\lambda}{[1 + (Y_b - Y_r)^2]^{1/2}} \right\} - \mu. \quad (12)$$

Equations (11) and (12) are to be solved with $Y_b(T_{jump}^-) = Y_b(T_{jump}^+)$, $\dot{Y}_b(T_{jump}^-) = \dot{Y}_b(T_{jump}^+)$ and $Y_r(T_{jump}^-) = \dot{Y}_r(T_{jump}^-) = 0$. This is expected to hold until $Y_b = -\Delta$, at some $T = T_{contact} = T_c$ at which point the central mass hits the substrate; then $R_b > 0$ to prevent penetration of the substrate and Phase 3 begins.

3. *Driven jump:* Once the central mass contacts the floor, the outer masses begin a more concerted jump, since the full force of the spring is now acting to push them upwards (the central mass can no longer move, i.e. $Y_b = -\Delta$) (see Fig. 6A (v)). In this phase, $R_r = 0$ is still fixed (since the outer masses remain out of contact with the floor).

Now it is *just* Y_r that is evolving, so that

$$M \frac{d^2 Y_r}{dT^2} = -\frac{1}{2} (\Delta + Y_r) \left\{ 1 - \frac{\lambda}{[1 + (\Delta + Y_r)^2]^{1/2}} \right\} - \mu, \quad (13)$$

with $Y_r(T_c^-) = Y_r(T_c^+)$, $\dot{Y}_r(T_c^-) = \dot{Y}_r(T_c^+)$. In this phase, the spring is relaxing towards its natural length and, in so doing, lifting the edges of the robot further off the ground. This phase continues as long as $R_r > 0$, which in turn requires that the spring remains compressed, i.e.

$$(\Delta + Y_r) \left\{ \frac{\lambda}{[1 + (\Delta + Y_r)^2]^{1/2}} - 1 \right\} > 0. \quad (14)$$

So, phase 3 ends when

$$Y_r = \sqrt{\lambda^2 - 1} - \Delta = Y_{r,take-off}. \quad (15)$$

At this point, the central mass would require an adhesive contact force to stay in touch with the substrate and (in its absence) instead takes off.

4. *Total loss of contact:* Once $R_r = R_b = 0$, the whole robot (both central and outer masses) has lost contact with the substrate and therefore takes off from the floor (see Fig. 6A (vi)). In this phase, the robot is subject just to the external force of gravity and so behaves as a projectile, albeit with a weak oscillation induced by the tension and compression of the spring.

Both central and edge masses are moving again, so we have

$$\frac{d^2 Y_b}{dT^2} = -(Y_b - Y_r) \left\{ 1 - \frac{\lambda}{[1 + (Y_b - Y_r)^2]^{1/2}} \right\} \quad (16)$$

and

$$M \frac{d^2 Y_r}{dT^2} = \frac{1}{2} (Y_b - Y_r) \left\{ 1 - \frac{\lambda}{[1 + (Y_b - Y_r)^2]^{1/2}} \right\} - \mu. \quad (17)$$

Equations (16) and (17) are to be solved with $Y_r(T_{take_off}^-) = Y_r(T_{take_off}^+)$, $\dot{Y}_r(T_{take_off}^-) = \dot{Y}_r(T_{take_off}^+)$ and $Y_b(T_{take_off}^-) = -\Delta$; $\dot{Y}_b(T_{jump}^-) = 0$. This phase is expected to hold until $Y = 0$ $Y=0$ again (at which point the robot lands).

By applying appropriate initial conditions, we can solve the motion equations at different stages in turn to quantitatively predict the jumping motion. More specifically, at each stage, the differential equations of motion can be solved numerically by employing the routine ode15s in Matlab. All the (physical and geometric) parameters are measured from experiments (as given in Table S1), except for the spring stiffness. The approximate value of the stiffness can be estimated by equating the stored energy in the latched state of the model system with that in the real robot: we assume the maximum energy in the von-Mises truss is equal to the elastic energy stored in the beam when the snapping beam passes the critical (fold) point. Since we are considering four designs of robot in experiments with different physical and geometric parameters, we treated the exact value of the spring stiffness as a single fitting parameter for all four robots (Fig. 6 B and C). This fit is performed once for all, with the value of k fixed as the restriction height changes.

Analytical results for Phase 3

In Phase 3, $Y_b = -\Delta$ is fixed and so we are able to make some analytical progress in determining, in particular, the evolution of the edge heights and the final jumping speed. We have that (recalling eq. (13))

$$M \frac{d^2 Y_r}{dT^2} = -\frac{1}{2} (\Delta + Y_r) \left\{ 1 - \frac{\lambda}{[1 + (\Delta + Y_r)^2]^{1/2}} \right\} - \mu. \quad (18)$$

To simplify the problem, we assume that the edges have not moved significantly by the start of phase 3, i.e. $Y_r(T_c^-) \approx \dot{Y}_r(T_c^-) \approx 0$, corresponding to no significant acceleration in Phase 2.

For notational convenience, we let $\tilde{Y}_r = Y_r + \Delta$, so that

$$M \frac{d^2 \tilde{Y}_r}{dT^2} = -\frac{1}{2} \tilde{Y}_r \left\{ 1 - \frac{\lambda}{(1 + \tilde{Y}_r^2)^{1/2}} \right\} - \mu, \quad (19)$$

with $\tilde{Y}_r(T_c^-) = \Delta$, $\dot{\tilde{Y}}_r(T_c^-) = 0$.

We can proceed by multiplying through by $d\tilde{Y}_r/dT$ and integrating, which gives,

$$M \frac{1}{2} \left(\frac{d\tilde{Y}_r}{dT} \right)^2 = \frac{1}{2} \lambda (1 + \tilde{Y}_r^2)^{1/2} - \frac{1}{4} \tilde{Y}_r^2 - \mu \tilde{Y}_r - \left[\frac{1}{2} \lambda (1 + \Delta^2)^{1/2} - \frac{1}{4} \Delta^2 - \mu \Delta \right]. \quad (20)$$

Recalling from the earlier analysis that take-off of the edge masses happens when the spring is no longer stretched, i.e., $Y_r = Y_r^{crit} = \sqrt{\lambda^2 - 1} - \Delta$ or $\tilde{Y} = \sqrt{\lambda^2 - 1}$, we find that the final jump speed satisfies

$$V_{jump}^2 = \left\{ \lambda \left[\lambda - \sqrt{1 + \Delta^2} \right] - \frac{1}{2} (\lambda^2 - 1 - \Delta^2) - 2\mu (\sqrt{\lambda^2 - 1} - \Delta) \right\} / M, \quad (21)$$

where V_{jump} is the non-dimensional velocity, which is related to the dimensional velocity through

$$v_{jump} = \frac{w}{t^*} \cdot V_{jump} \quad (22)$$

with $t^* = \sqrt{m_b/2k}$ as a time scale as we defined before. By combining Eq. (21) and (22) and recalling the various dimensionless parameters that have been introduced, we can therefore obtain the dimensional velocity with respect to the restriction height, i.e.,

$$v_{jump}^2 = \frac{2k}{m_r} \cdot \left\{ l_0 \left[l_0 - \sqrt{w^2 + \left(\sqrt{l_0^2 - w^2} - h_R \right)^2} \right] - \frac{1}{2} \left[l_0^2 - w^2 - \left(\sqrt{l_0^2 - w^2} - h_R \right)^2 \right] - 2\mu_0 h_R \right\}, \quad (23)$$

This expression agrees well with numerical results of the full model as presented in the paper, despite the neglect of the 'ghost jump' phase of the motion. In particular, we find that the dependence of take-off velocity v_{jump} on restriction height h_R tends to be linear as $h_R \rightarrow 0$, while $v_{jump} \rightarrow const$ when $h_R \rightarrow h_0$. To understand this better, we seek insight from an energetic perspective. For small restriction heights ($h_R \rightarrow 0$), contact occurs well after snap-through; the kinetic energy of the beam at the moment of impact is dissipated and we therefore suppose that only the elastic energy remaining in the buckled beam at the moment of collision is transferred to kinetic energy of the robot, i.e.,

$$2 \cdot \frac{1}{2} m_r v_{jump}^2 = 2 \cdot \frac{1}{2} k \left(l_0 - \sqrt{d^2 + w^2} \right)^2, \quad (24)$$

where $d = h_0 - h_R$. We can therefore simplify this equation as

$$v_{jump} \approx \sqrt{\frac{k}{m_r} \frac{h_0}{l_0}} \cdot h_R \propto h_R \quad (25)$$

Conversely, for large restriction heights ($h_R \rightarrow h_0$), contact occurs almost immediately after snap-through and so all the elastic energy initially stored in the buckled beam is transferred into the robot as kinetic energy,

$$2 \cdot \frac{1}{2} m_r v_{jump}^2 = 2 \cdot \frac{1}{2} k (l_0 - w)^2, \text{ so} \quad (26)$$

$$v_{jump} \approx \sqrt{\frac{k}{m_r}} (l_0 - w) \square const. \quad (27)$$

These intuitive results are recovered as the appropriate limits of equation (23).

Alternative model to analyze the robot's jumping: a simple linear harmonic oscillator

We investigate the use of a simple linear harmonic oscillator as an alternative model to analyze the robot's jumping (Fig. S5A). The robot is modeled by two masses vertically connected by a spring. The lower mass m_b and the spring represent the buckling beam, but taken to be a linear spring. The upper mass m_r is equivalent to the mass of the robot body. The model assumes a massless spring. At the initial state, both m_r and m_b are fixed such that the spring is compressed by a displacement D , representing the equivalent compression of the buckled beam. The distance between m_b and the ground is H . The jump is initiated by releasing m_b , while keeping m_r fixed, and the process of jumping evolves through two distinct phases, as illustrated schematically in Fig. S5B.

1. *Lower mass snapping:* The motion begins when m_b is released by removing a trigger. During this phase, the robot mass (m_r) is still fixed at its initial position by an external force, and the restoring force of the spring pushes m_b downwards towards the ground. This phase corresponds to Phase 1 in the Von Mises truss model, when the central mass is snapping downwards. The parameters are selected such that m_b reaches the ground while the spring is still compressed.
2. *Driven jump:* At the instance of collision between m_b and the ground, the constraint on m_r is removed. The robot mass m_r has a high instantaneous acceleration due to the sudden removal of the constraint, and begins moving upwards due to the restoring force of the compressed spring during collision. This collision process is similar to Phase 3 (driven jump) defined in the Von Mises truss model.
3. *Total loss of contact:* The entire assembly (both m_r and m_b) takes off from the ground when m_b fully rebounds after collision. The assembly then follows an upwards projectile motion, and this phase is similar to Phase 4 in the Von Mises truss model.

The equation of motion of m_b for phase 1 can be expressed as

$$y_b(t) = \left(D + \frac{m_b g}{k}\right) \cos(\omega_b t), \quad (28)$$

where m_b is the beam mass, y_b is the displacement of m_b , D is the compression of the spring, and k is the spring constant.

The beam mass m_b hits the ground with a pre-collision velocity of v_0 . It remains on the ground for a collision time t_c and rebounds with another velocity by a coefficient of restitution (COR) due to energy loss during the collision. This impulse makes a significant impact in pushing against the ground and propelling the robot into the air. During the collision process, the equation of motion of the robot mass m_r can be expressed as

$$y_r(t) = \left(L - \frac{m_r g}{k} + \frac{m_b g}{k} + D - H\right) \left(\frac{\alpha_r}{\omega_r}\right) \left(D - H - \frac{m_r g}{k}\right) \cos(\omega_r t_c), \quad (29)$$

where m_r is the robot mass, y_r is the displacement of m_r , D is the compression of the spring, L is the original length of the spring, H is the distance between m_b and the ground at the initial state before phase 1 starts, k is the spring constant, and $\alpha_r = \sqrt{\frac{k}{m_r}}$.

After total loss of contact with the ground, the robot experiences a constant gravitational force. Neglecting subsequent oscillations of the spring, the two masses will move up together until they reach the maximum jumping height. The center of mass movement after takeoff can be obtained as

$$Y(t) = Y_0 + V_0 t' - \frac{1}{2} g(t')^2, \quad (30)$$

where $Y = \frac{m_r y_r}{M} + \frac{m_b y_b}{M}$ is the position of the entire system written in the center-of-mass coordinates, $M = m_r + m_b$ is the total mass, Y_0 is the position of the system at the end of the collision, $V_0 = \frac{m_r}{M} v_0$ is the velocity of the system at the end of the collision, and v_0 is the end velocity of m_b after rebounding from collision.

We compare the acceleration evolution of the simple harmonic model with that of the more accurate Von Mises truss model and experimental measurements in Fig. S5B. An accurate feature of the Von Mises truss model is its ability to capture the sharp but continuous rise in the robot's acceleration during the lower's mass collision with the ground. The simple harmonic model has a discontinuous acceleration that starts at the maximum value because the constraint which fixes m is removed at the instant when collision starts. At $t = 0$ in Fig. S5B, the upper mass m_r is only subjected to the spring force and its own gravity due to sudden removal of the constraint. Moreover, the evolution of the acceleration, namely the convex decrease during takeoff, can be captured by the Von Mises truss model. Unfortunately, our high-speed camera system did not allow accurate noise-free measurement of this acceleration.

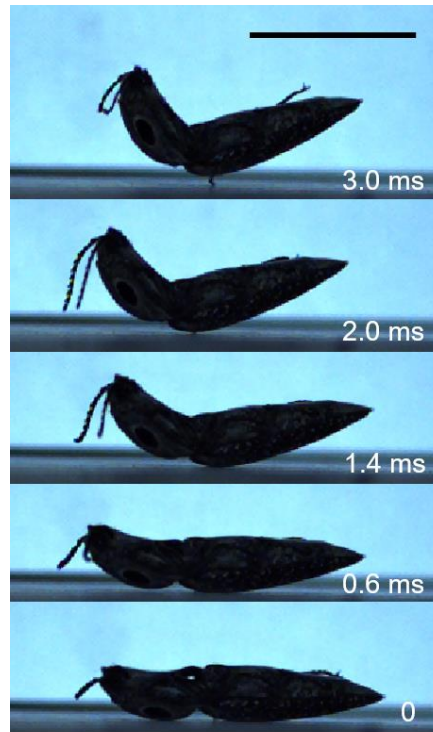


Fig. S1. Snapshots of the takeoff sequence of an *Alaus oculatus* click beetle. The snapshots show the extremely fast unbending movement which results in the center of mass acceleration and legless jump. The mass of the click beetle is 754 mg, and the body length is 31 mm.

The key steps of our evolutionary design are shown in Fig. S2, and described below.

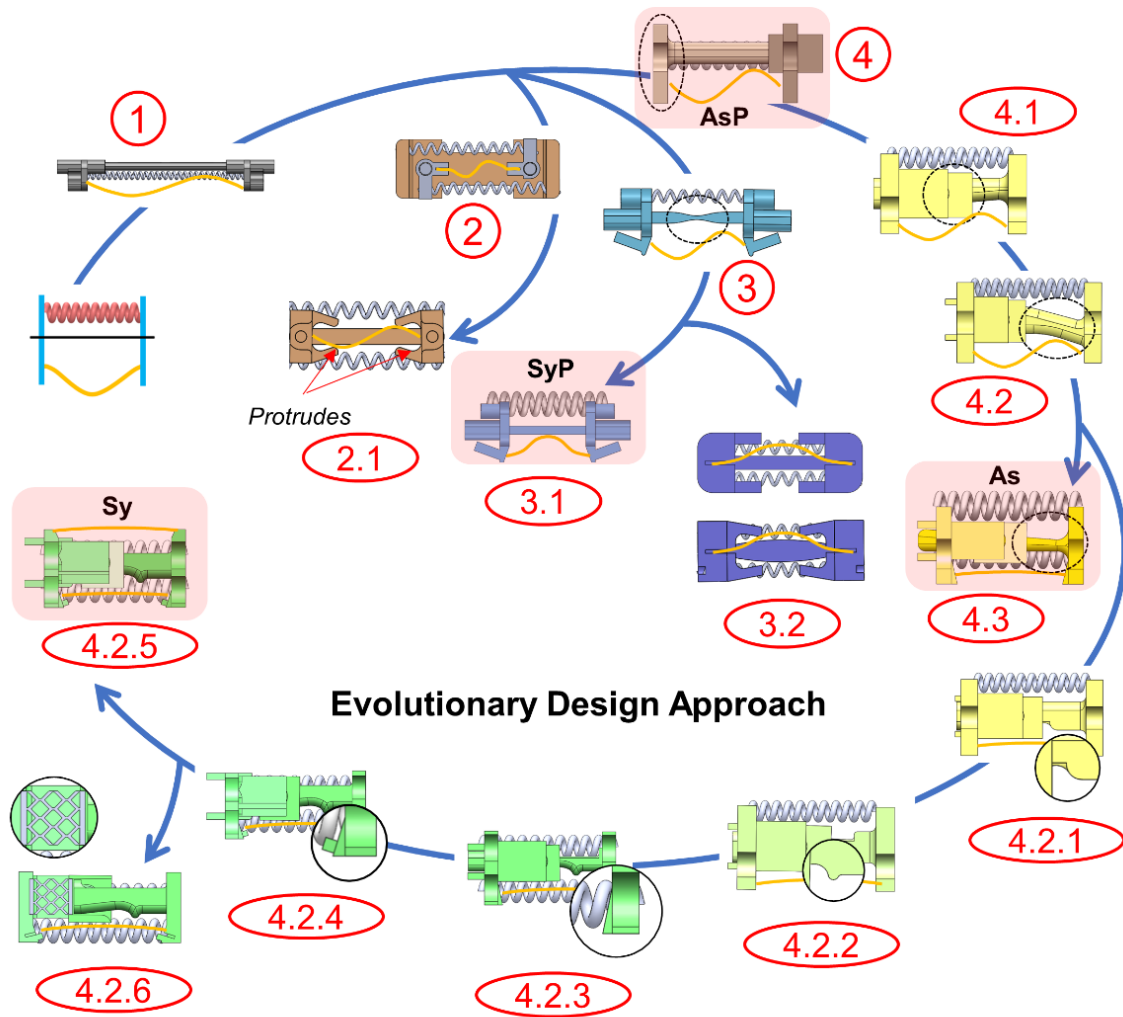


Fig. S2. Evolutionary design approach. Key steps in the evolution of our robot are indicated by numbers as follows:

(1) The first jumping robot design, which originated from the initial concept, consists of a sliding bar, a pair of artificial muscles, and a buckling beam, triggered by the translation of the two clamps due to the compressive force of the muscles.

(2) Jumping robot design with a triggering mechanism based on the rotation of the two ends of the buckled beam instead of translation.

(2.1) Design that evolved from (2). Protrusions parallel and near the ends of the beam are used to push the beams and trigger snap-through at a smaller angle of clamp rotation and hence accommodating smaller muscle stroke.

(3) Jumping robot design without sliding bar but with a fixed bendable bar. When the robot body is bent by the compressive stroke of the muscle, the buckled beam is rotated from its two ends until snap-through.

(3.1) The bendable bar is thickened and re-designed to avoid fracture upon bending. The buckled beam has a symmetrical shape to store more energy. Mandrel-coiled artificial muscles are used to provide larger force and stroke.

(3.2) Other robot designs evolved from (3). The robots are fabricated using more flexible materials.

(4) Jumping robot design with a single-side sliding mechanism to compress the beam and trigger snap-through. The length of the robot is also shortened compared to (1) to achieve a smaller footprint robot design.

(4.1) The bottom of the sliding bar has an inclined surface. Upon actuating the artificial muscles, the upper side of the robot body will shrink more than the lower side, triggering the snap-through of the buckled beam. A rotational block is added to push and help triggering snap-through.

(4.2) A bent sliding bar is added to guide the rotation of the small block.

(4.2.1) A rounded corner is designed to replace the bent sliding bar, which rotates the small block and triggers snap-through during compression.

(4.2.2) A protrusion is designed to replace the rounded corner for tailoring snap-through.

(4.2.3) The size and weight of the robot are reduced. Inclined beam clamping is introduced to ensure the beam can buckle upwards upon compression.

(4.3.4) A small protrusion is designed on the inclined beam clamping to introduce initial bending to the beams before compression. This is to ensure the beam can always buckle upwards for consecutive jumping.

(4.2.5) A top beam is introduced to restore energy for consecutive jumping.

(4.2.6) An architected spring is introduced to restore energy for consecutive actuation.

(4.3) Four mandrel-coiled artificial muscles are used to compress the beam. The beam is able to be compressed from its energy-free state. The sliding bar is designed to be thinner to reduce the self-weight of the jumping robot.

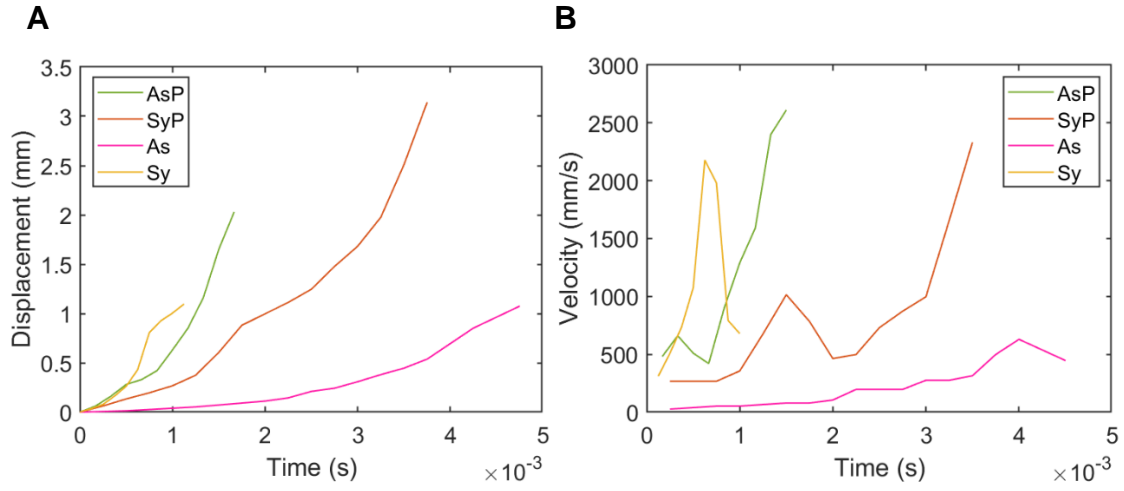


Figure S3. Displacement (A) and velocity (B) of the central point of the buckled beam during the snap-through process for all four cases. For cases with asymmetrical beams, both displacement and velocity were measured by tracking the points that reach the ground last. For cases with symmetrical beams, displacement and velocity were measured for the points which hit the ground first.

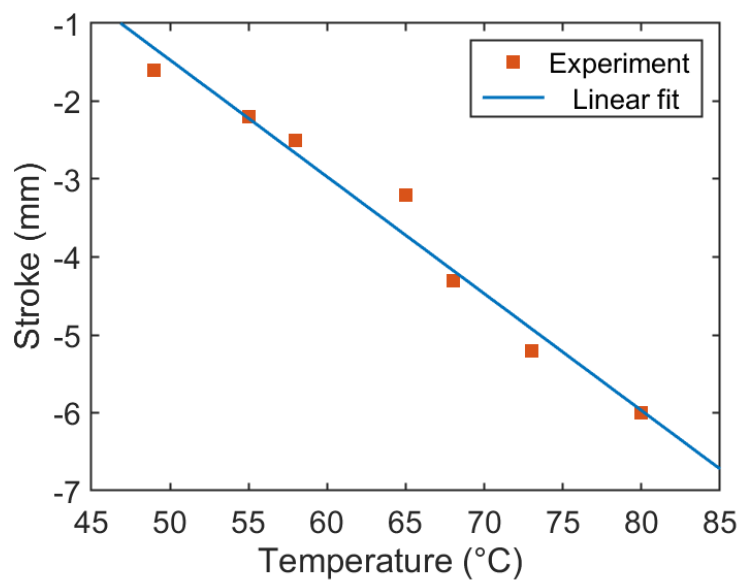


Figure S4. Plot of stroke versus temperature of the artificial muscle. The muscle was made of 1 mm fishing line. The original length of the muscle is 27 mm with a constant load of 200 g fixed at one end.

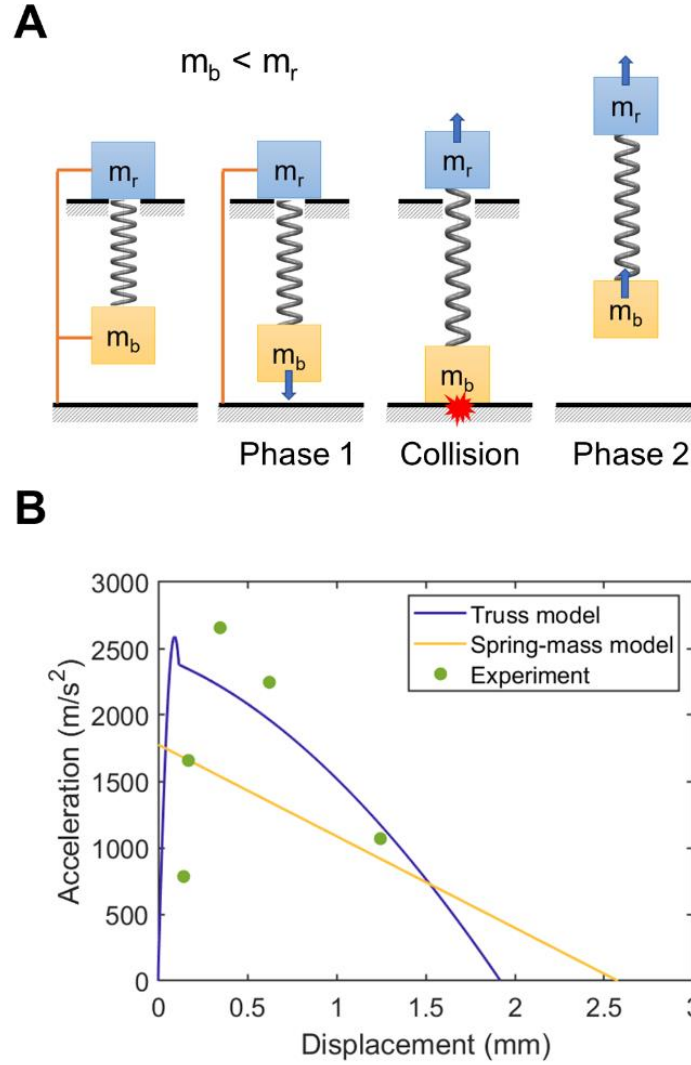


Figure S5. Reduced-order model of the robot jumping mechanism using a linear mass-spring oscillator. (A) Schematic of the linear mass-spring oscillator model used to analyze the robot jumping mechanism. This model uses rigid holders, shown in orange, that constrain the motion of the masses while the energy is stored in the spring (left frame), then release and trigger the motion of m_b , while still constraining m_r in phase 1, and then release m_r when collision takes place. (B) Comparison between the measured acceleration of the robot as a function of jumping displacement with that predicted by the Von-Mises truss model and the spring-mass model.

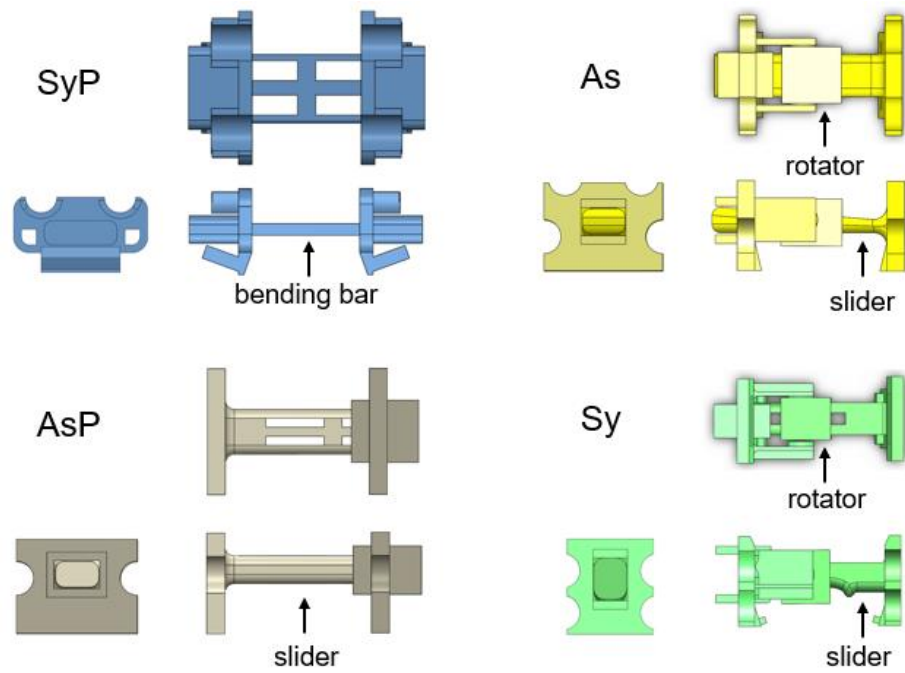


Figure S6. 2D views of the four robot designs (front view, side view, top view).

Table S1. Design parameters of all four jumping robots.

| Robot | Robot weight [g] | Robot size [mm] | No. of muscles | Beam size [mm] | Beam weight [g] |
|--------------|-----------------------------|----------------------------|---------------------------|---------------------------|----------------------------|
| AsP | 1.66 | 23.5×14×11 | 2 | 25.5×6.4×0.0508 | 0.063 |
| SyP | 1.68 | 26×17×9.8 | 2 | 15.9×6.6×0.0508 | 0.062 |
| As | 1.83 | 22×13.5×10 | 4 | 16.3×6.5×0.0508 | 0.050 |
| Sy | 1.58 | 21.5×10×10.5 | 4 | 15.7×5.3×0.0508 | 0.061 |

Table S2. Parameters and jumping performance of small-size jumping robots in the literature.

| S/N | Body length [mm] | Jump Height [m] | Acceleration [m/s ²] | Body Weight [g] | Reference |
|-----|------------------|-----------------|----------------------------------|-----------------|-----------|
| 1 | 25 | 0.1 | 42.5 | 22 | (16) |
| 2 | 75 | 0.87 | - | 26.5 | (44) |
| 3 | 90 | 1.44 | - | 25 | (15) |
| 4 | 130 | 3.35 | - | 23 | (45) |
| 5 | 120 | 1.5 | 750 | 99 | (46) |
| 6 | 150 | 1.25 | 140 | 98 | (14) |
| 7 | 90 | 0.21 | - | 54.1 | (42) |
| 8 | 50 | 1.4 | 397.33 | 7 | (43) |
| 9 | 20 | 0.142 | 138 | 0.068 | (48) |
| 10 | 23 | 0.64 | 500 | 1.1 | (47) |
| 11 | 41 | 0.15 | - | 18 | (41) |

Table S3. Parameters and jumping performance of jumping robots in this work.

| Robot | Body length [mm] | Jump Height [m] | Acceleration [m/s²] | Body Weight [g] |
|--------------|-----------------------------|----------------------------|---|----------------------------|
| AsP | 23.5 | 220 | 931 | 1.66 |
| As | 22 | 50 | 227 | 1.83 |
| Sy | 21.5 | 170 | 482 | 1.58 |
| SyP | 23.1 | 237 | 1471 | 1.68 |
| Syp+2 | 23.1 | 279 | 1574 | 1.686 |
| SyP+3 | 23.1 | 406 | 1899 | 1.692 |
| SyP+4 | 23.1 | 712 | 2156 | 1.698 |
| SyP+5 | 23.1 | 893 | 2414 | 1.704 |

Table S4. Parameters and jumping performance of insects in the literature.

| Insect Name | Body Length [mm] | Jumping Height [mm] | Acceleration [m/s ²] | Body weight [mg] | Reference |
|---|------------------|---------------------|----------------------------------|------------------|-----------|
| <i>Philaenus Spumarius</i> froghopper | 6.1 | 428 | 2800 | 12.3 | (3) |
| <i>Archaeopsyllus erinacei</i> flea | 1.8 | 34 | 1600 | 0.7 | (9) |
| Snow Flea (Male) | 3.4 | 19 | 121 | 2.9 | (4) |
| Snow Flea (Female) | 4.2 | 17 | 161 | 4.2 | |
| <i>Aphrodes makarovi</i> leafhopper | 8.5 | 115 | 1055 | 18.4 | |
| <i>Saldula saltatoria</i> Shore Bug | 3.5 | 53 | 529 | 2.1 | |
| <i>Ulopa</i> | 3.1 | 127 | 2300 | 2.1 | (10) |
| <i>Cephalelus</i> | 13.4 | 90 | 1000 | 9.2 | |
| <i>Publilia concava</i> (Female) treehopper | 4.7 | 126 | 1500 | 4.5 | (37) |
| <i>Publilia concava</i> (male) treehopper | 4.1 | 195 | 1690 | 3.8 | |
| <i>Entylia carinata</i> (Female) treehopper | 4.6 | 128 | 1750 | 5.9 | |
| <i>Entylia carinata</i> (male) treehopper | 4.2 | 170 | 2080 | 4.8 | |
| <i>Campylenchia latipes</i> (Female) treehopper | 7.8 | 85 | 1230 | 10.3 | |
| <i>Sextius sp</i> treehopper | 6.9 | 108 | 1220 | 18.7 | |
| <i>Carynota marmorata</i> treehopper | 7.2 | 177 | 960 | 25 | |
| <i>Stictocephala bisonia</i> treehopper | 7.8 | 135 | 770 | 26.8 | |
| <i>Ceresa basalis</i> treehopper | 6.9 | 72 | 590 | 28.5 | |
| <i>Telamona compacta</i> treehopper | 8.4 | 80 | 560 | 41 | |
| <i>Panorpa communis</i> (Female) Fly | 15.1 | 46 | 95.5 | 39.7 | (38) |
| <i>Panorpa communis</i> (male) Fly | 13.2 | 46 | 65.5 | 26.7 | |
| <i>Idaea seriata</i> small dusty wave moth | 6.8 | 19 | 88 | 4.6 | (39) |
| <i>Hofmannophila pseudospretella</i> brown house-moth | 9.1 | 33 | 71 | 5.4 | |
| <i>Acleris sparsana</i> ashy button moth | 7 | 27 | 40 | 6.3 | |
| <i>Epiphyas postvittana</i> light brown apple moth | 7 | 34 | 92 | 7.7 | |

| | | | | | |
|---|------|------|------|-------|------|
| <i>Crambus pascuella</i> grass veneer moth | 9.2 | 24 | 37 | 11.9 | |
| <i>Campptogramma</i> <i>bilineata</i> yellow shell moth | 10.3 | 49 | 61 | - | |
| <i>Xanthorhoe fluctuate</i> garden carpe moth | 10 | 47 | 57 | 17.4 | |
| <i>Udea olivalis</i> olive pearl moth | 10.8 | 44 | 42 | 19.1 | |
| <i>Apamea lithoxylaea</i> light arches moth | 18.3 | 26 | 29 | 220.9 | |
| <i>Microtechnites</i> <i>bractatus</i> (female) mirid | 2.7 | 24 | 35 | 3.4 | (40) |
| <i>Orthocephalus saltator</i> mirid | 3.2 | 9 | 76 | 4.4 | |
| <i>Phytocoris</i> <i>varipes</i> (male) mirid | 5.6 | 27 | 85 | 7.9 | |
| <i>Phytocoris</i> <i>varipes</i> (female) mirid | 6.4 | 36 | 99 | 12.2 | |
| <i>Plagiognathus</i> sp mirid | 3.9 | 18 | 63 | 2.2 | |
| <i>Tettigoniidae</i> Locust | 35 | 230 | - | 420 | (11) |
| Click beetle | 20.3 | 300 | 3724 | 200 | (35) |
| <i>L. biguttatus</i> | 5.22 | 14.2 | 179 | 1.3 | (36) |
| Trap jaw ants mean | ~10 | 73 | 4720 | 13.5 | (1) |
| Trap jaw ants max | ~10 | 83 | 8800 | 12.1 | |
| Trap jaw ants min | ~10 | 61 | 2410 | 14.9 | |

Table S5. Mass distribution of the untethered jumping robot.

| Total (g) | PCB (g) | Battery (g) | Frame (g) | Sensor Circuit (g) | Muscle (g) | Beams (g) |
|-----------|---------|-------------|-----------|--------------------|------------|-----------|
| 13.561 | 7.535 | 3.011 | 1.139 | 0.862 | 0.758 | 0.256 |

Autonomy of miniature jumping robots

Inspired by the definitions of “full self-driving” issued by the Society of Automotive Engineers SAE J3016, the robots described in this paper are autonomous, but not yet “fully autonomous”. The SAE defines 6 levels of autonomy for self-driving vehicles, starting from Level 0 - no automation; to Level 1 - hands on/shared control; and going up all the way to Level 5, where the existence of a steering wheel is considered optional in future vehicles. We propose definitions of the levels of autonomy of insect-scale robots in Table S6.

Table S6. The levels of autonomy of insect-scale robots.

| Autonomy Level for jumping robots | 0 | 1 | 2 | 3 | 4 | 5 |
|-----------------------------------|----------------|-------------------------------|------------------|------------------|----------------|-------------------|
| Function | On board power | Self-generated elastic energy | On-board sensing | On-board command | Re-orientation | Consecutive jumps |
| Robots in this manuscript | Yes | Yes | Yes | Yes | No | Partial |

Evolution *versus* Trial-and-error in the Design Process

Our design process used features that are similar to both trial-and-error as well as evolution (natural selection). In trial-and-error design process, a new trial is typically directed by knowledge acquired in the previous iteration. For instance, if the actuator is found by the researchers to be inadequate or too weak, a new stronger actuator is used in the next iteration. The next trial is directed by empirical observations made based on the failure of the previous generations, and hence is not entirely random, which sets it apart from a mutation in natural evolution. On the other hand, when a new trial is successful, the new feature is maintained in the following mutation which indicates that future generations inherit these survival and fitness traits – a common element of both the trial-and-error approach and natural evolution. Survival is defined by the robot ability to jump (binary) and not fracture (also binary).

The design process used in this study has two other elements reminiscent of natural evolution, and uncommon in engineering trial-and-error. First, the starting seeds were randomly selected and hence had unpredictable performance. As shown in Fig. 2 of the main text, we started with an abstract concept of a robot having three components: a deformable robot body of arbitrary geometry, a coiled artificial muscle actuator, and an elastic energy storing component. Inspired by evolutionary processes observed in nature, we considered four randomly selected initial configurations. Like evolution, these initial seeds, or phenotypes, were not initially directed because

the complexity of the nonlinear mechanics and multi-physics of buckling, snap-through and fracture mechanics prohibited the performance predictability, especially those which would result after many trial-and-error cycles. The second element that is similar to natural evolution is the use of the same constituent components types throughout the trial-and-error process. No new components were added between iterations, which evolution would not typically do either. These components have tunable properties (e.g. the morphology of the beam, the muscle and the robot) which contributes to the ability of evolving this specific trait, similar the process of trait passing in natural evolution. These ideas are summarized in Table S7.

Table S7. Comparison among natural evolutionary processes, trial-and-error design methods, and our robot design process.

| Development process | Natural evolutionary processes | Trial-and-error design methods | Robot Design |
|--|---------------------------------------|---------------------------------------|--|
| Initial seed | Random | Guided/based on knowledge | Random ^a |
| Fitness landscape | Unpredictable | Moderately predictable | Unpredictable |
| Mutation | Random | Guided/directed | Partially guided/directed; Partially random ^b |
| Rate of trait passing (selection) | Rate of survival and reproduction | Error from target | Rate of survival and reproduction ^c |
| New generation | Inherits fitness traits | Inherits fitness traits | Inherits fitness traits |

^a Morphology and parameters of the design were selected randomly

^bThe robot with the central bending bar or the robot with the clamps rotation were not initially designed to have this elasticity, it was observed coincidentally due overheating (environmental effect) and it was subsequently maintained due to the jumping performance associated with it (fitness)

^cRate of survival and reproduction in the robots: survival is literally defined by robots which jump and not fracture; reproduction is defined as the ability of this trait (e.g. robot body, muscle, energy storing element) to being tunable.

Movie S1 (separate file). Jumping of SyP and SyP+ and high-speed camera close-up view of SyP jumping.

Movie S2 (separate file). Multiple jumping demonstration of Sy and a close-up of high-speed jumping of Sy.

Movie S3 (separate file). Jumping of SyP with electrically triggered muscles.

Movie S4 (separate file). Jumping of As and AsP, followed by high-speed camera close-up views of the robots.

Movie S5 (separate file). Tensile test and force-displacement relations of the four robots.

Movie S6 (separate file). Untethered jumping triggered by light stimuli. The vertical scale bar on the right represents the temperature.